Nano-Micro Letters

ISSN 2311-6706
e-ISSN 2150-5551
CN 31-2103/TB

ARTICLE

https://doi.org/10.1007/s40820-020-00461-x

Cite as
Nano-Micro Lett.
(2020) 12:125

Received: 31 March 2020
Accepted: 6 May 2020
Published online: 11 June 2020

A Flexible and Lightweight Biomass-Reinforced Microwave Absorber

Yan Cheng[1], Justin Zhu Yeow Seow[2,3], Huanqin Zhao[1], Zhichuan J. Xu[2,3] ✉, Guangbin Ji[1] ✉

Yan Cheng and Justin Zhu Yeow Seow have contributed equally to this work.

✉ Zhichuan J. Xu, xuzc@ntu.edu.sg; Guangbin Ji, gbji@nuaa.edu.cn

[1] College of Materials Science and Technology, Nanjing University of Aeronautics and Astronautics, Nanjing 210016, People's Republic of China

[2] School of Materials Science and Engineering, Nanyang Technological University, 50 Nanyang Avenue, Singapore 639798, Singapore

[3] Singapore-HUJ Alliance for Research and Enterprise, NEW-CREATE Phase II, Campus for Research Excellence and Technological Enterprise (CREATE), Singapore 138602, Singapore

HIGHLIGHTS

- A flexible and lightweight microwave absorber was prepared by a vacuum filtration method.
- The remarkable microwave absorbency makes the absorber paper attractive in wireless wearable electronics field.

ABSTRACT Developing a flexible, lightweight and effective electromagnetic (EM) absorber remains challenging despite being on increasing demand as more wearable devices and portable electronics are commercialized. Herein, we report a flexible and lightweight hybrid paper by a facile vacuum-filtration-induced self-assembly process, in which cotton-derived carbon fibers serve as flexible skeletons, compactly surrounded by other microwave-attenuating components (reduced graphene oxide and Fe_3O_4@C nanowires). Owing to its unique architecture and synergy of the three components, the as-prepared hybrid paper exhibits flexible and lightweight features as well as superb microwave absorption performance. Maximum absorption intensity with reflection loss as low as − 63 dB can be achieved, and its broadest frequency absorption bandwidth of 5.8 GHz almost covers the entire Ku band. Such a hybrid paper is promising to cope with ever-increasing EM interference. The work also paves the way to develop low-cost and flexible EM wave absorber from biomass through a facile method.

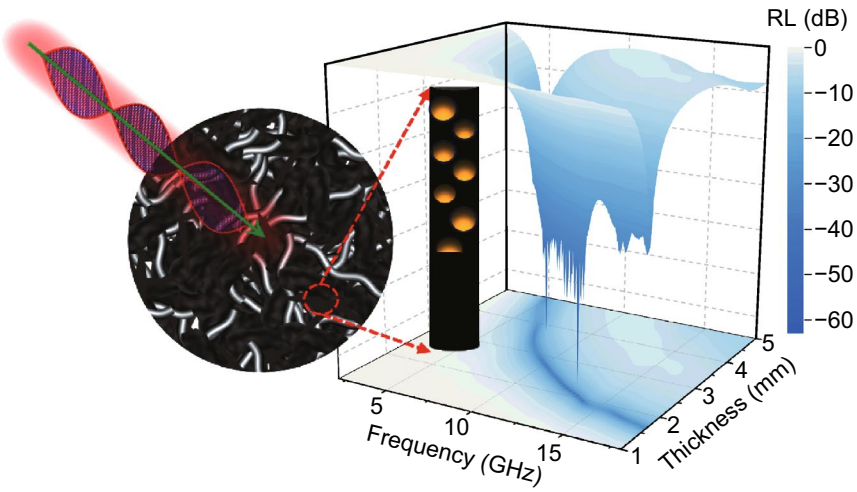

KEYWORDS Flexible; Biomass; Microwave absorption; Dielectric loss; Magnetic loss

1 Introduction

Wireless electronics, especially wearable electronics, have attracted growing public attention through recent technology advances. With increasing expectation on the efficiency of such electronics, sensitivity of these electronics to input signals needs to be improved while decreasing their susceptibility to unwanted environmental interference [1, 2]. A viable solution to serious signal interference from electronics nearby is proposed, in which an electromagnetic (EM) absorption layer is directly attached to the surface of an electronic device [3]. The EM absorption layer is able to transform the unwanted EM energy into thermal energy and/or other energy forms, protecting the electronic equipment from signal interference. An aspect from the EM wave absorption capability and flexibility is required in an EM absorber to allow it to adapt to the shape of wearable electronics [4]. Although traditional binder-containing microwave absorbers have made great progress toward high absorption efficiency, they are still hardly used practically because of their lack of stability and poor mechanical properties [5].

Recent progress demonstrates that mixing conductive filler (such as carbon nanotube (CNT) and graphene) with polymer to create a composite film is a feasible strategy for flexible microwave absorption [6, 7]. In such setup, high content of conductive filler is necessary to build a conductive network and achieve adequate microwave absorptivity [8]. However, with high content of conductive fillers, the fillers tend to aggregate, jeopardizing mechanical property of the absorber [9]. As such, an alternative design of EM absorber involving the replacement of either the filler, the matrix or the microstructure of the composite is highly desired.

Commercial carbon cloth is a simple and widely used flexible substrate. Some impressive achievements of carbon-cloth-based flexible absorber have been recently reported. For example, Che et al. deposited MnO_2 arrays on a carbon cloth substrate, producing a flexible EM wave absorber that achieved RL of -53.2 dB by modifying phase structure and geometrical shape of the MnO_2 array [10]. Lately, Che's group also designed ZnO arrays vertically grown in situ on a flexible conductive carbon cloth substrate, producing EM wave absorbers with superior mechanical properties and enhanced EM attenuation ability [11]. These works have proven that carbon cloth is an ideal skeleton for a flexible EM wave absorber. Unfortunately, commercial carbon cloth is an expensive raw material, hindering commercialization of such inventions.

Cotton, a renewable biomass resource, has a fiber microstructure like carbon cloth in addition to other advantages including superior mechanical strength, low mass, low cost and high natural abundance [12]. More importantly, cotton-derived carbon fibers (CF) do not only inherit these fascinating merits, but also exhibit strong dielectric loss ability [13]. However, dielectric loss of the CF alone is unable to provide sufficiently remarkable microwave absorption for practical uses, making its integration with other components critical in achieving high microwave absorption performance from the synergy between different components [14, 15].

In pursuit of high-performance absorbers, graphene-based magnetic materials are widely studied due to their lightweight feature and their dual energy attenuation mechanisms, namely dielectric and magnetic losses [16]. For example, Fe_3O_4–graphene heterostructures exhibited superior RL of − 46.4 dB at thickness of as low as 1.4 mm [17]. Despite their strong microwave absorption abilities, these powder-like materials are lack of flexibility and cannot be used in portable electronics.

In attempt to address the mentioned challenges, we have synthesized a cotton-derived, carbon-fiber-reinforced hybrid paper made of reduced graphene oxide (rGO) and Fe_3O_4@C nanowires through facile vacuum filtration assembly. The tuning of the content of CF could modulate optimal thickness of the paper and optimize its impedance matching for different purposes. Finally, the produced paper shows good flexibility, lightweight feature and outstanding microwave absorption, exhibiting a promising prospect for its use in protecting wearable electronics.

2 Experimental

2.1 Materials

Cotton was purchased from a local supermarket in Jiangsu province, China. Iron(II) chloride tetrahydrate ($FeCl_2{\cdot}4H_2O$), nitrilotriacetic acid and isopropyl alcohol were purchased from Nanjing Chemical Reagent Co., Ltd.

https://doi.org/10.1007/s40820-020-00461-x

and used as received. The aqueous solution of dispersed graphene oxide nanosheets (GO, 2 mg mL^{-1}) and absolute ethanol were procured from Nanjing Crystal Chemical Co. Ltd.

2.2 Preparation of Carbon Fiber

Typically, 3 g cotton was loaded in a tube furnace and heated at 300 °C for 2 h with a heating rate of 5 °C min^{-1} in air. After carbonization, the obtained bulk CF was first cut into tiny pieces and then dispersed in ethanol to form a homogeneous dispersion with a density of 4 mg mL^{-1} before use.

2.3 Synthesis of Fe-CPNWs

Iron-based coordination polymer nanowires (Fe-CPNWs) were prepared via a facile hydrothermal synthesis. In detail, under vigorous stirring, 3.0 g of $FeCl_2{\cdot}4H_2O$ and 0.9 g of nitrilotriacetic acid were dissolved in 60 mL mixture of isopropyl alcohol and deionized water (DI, 0.3 MΩ cm) with a volume ratio of 1:1. The resulting solution was transferred into a 100-mL Teflon-lined stainless steel autoclave, which was placed in an oven for heating at 180 °C for 9 h. A white solid was formed after heating, which was later washed with DI water and ethanol for several times and then dried at 60 °C for 12 h under vacuum.

2.4 Preparation of Fe_3O_4@CNW/rGO/CF Hybrid Films

The as-prepared Fe-CPNWs were dispersed in absolute ethanol and sonicated for 15 min to form a homogeneous dispersion with a density of 1 mg mL^{-1}. Then, 12.5 mL of GO solution (2 mg mL^{-1}) was mixed with 250 mL of Fe-CPNW-containing ethanol solution, followed by the addition of different volumes of CF-containing ethanol solution (0, 20, 30 and 40 mL). After the solutions were mixed and sonicated for another 30 min, the mixture was left standing for 12 h and then filtered to obtain CF/GO/Fe_3O_4@CNW paper. The resultant composite paper was dried under ambient conditions and then carefully removed from the filter paper. Finally, it was placed in a tube furnace, heated with a ramp rate of 2 °C min^{-1} to 600 °C and kept for 3 h in Ar. Upon cooling down to room temperature, the final flexible CF/rGO/Fe_3O_4@CNW hybrid paper was obtained. In this article, the obtained hybrid papers with CF contents of 0, 20, 30 and 40 mL are denoted as S0, S1, S2 and S3, respectively.

2.5 Characterization

Microstructures and morphologies were observed using a Hitachi S4800 scanning electron microscope (SEM) and a JEOL JSM-2010 transmission electron microscope (TEM). X-ray powder diffraction (XRD) was performed on a Bruker D8 ADVANCE diffractometer. Raman spectra were recorded using a Renishaw inVia 2000 Raman microscope. X-ray photoelectron spectroscopy (XPS) system with PHI 5000 Versa Probe was used to obtain XPS spectra. Chemical bonding in the samples was analyzed using Fourier-transform infrared (FTIR) spectra, which were recorded by a PerkinElmer 2000 FTIR spectrometer using KBr disks. Thermogravimetry (TG) analysis was conducted using an NETZSCH STA 449F3 thermal gravimetric analyzer with the temperature ranging from 23 to 800 °C in air. The EM absorption parameters were measured via an Agilent PNA N5244A vector network analyzer in the frequency range of 2–18 GHz according to the coaxial-line method. The tested specimens were prepared by homogeneously mixing the paraffin wax with samples at sample-to-wax mass ratio of 2: 8 and then pressing the mixture into toroidal-shaped ring with outer diameter Φ_{out} of 7.00 mm and inner diameter Φ_{in} of 3.04 mm.

3 Results and Discussion

The cotton was first treated at a low temperature of 300 °C in air to obtain CF with oxygen-containing functional groups. Figure S1a reveals that the CF has a smooth surface with a diameter of several micrometers. FTIR spectrum of CF is shown in Fig. S1b. The broad peak at around 3400 cm^{-1} is associated with stretching vibrations of OH groups [18]. The peaks at 1705 and 1618 cm^{-1} belong to stretching vibrations of C=O and C=C, respectively [19]. The peak at 1243 cm^{-1} corresponds to stretching vibration of carboxylic anhydride groups [20]. The results confirm that the low-temperature carbonization in air resulted in formation of oxygen-containing functional groups in CF.

Simultaneously, Fe-CPNWs were synthesized using a solvothermal method in a Teflon-lined stainless-steel autoclave. Figure S1c demonstrates that Fe-CPNWs possess

well-defined one-dimensional structures with a mean diameter of about 160 nm. The corresponding FTIR spectrum discloses the composition of Fe-CPNWs (Fig. S1d). The peak cantered at 3437 cm^{-1} is ascribed to the coordination between Fe^{2+} and nitrilotriacetic acid [21]. The peak at about 1593 cm^{-1} belongs to in-plane bending vibration of N–H bond. The peaks at about 1303 and 1028 cm^{-1} are assigned to the stretching vibration and in-plane bending vibration of C-H bond, respectively [22]. GO aqueous solution was homogeneously mixed with Fe-CPNW-containing ethanol solution and CF-containing ethanol solution. In this process, CFs interacted with GO nanosheets through their oxygen-containing functional groups by means of van der Waals forces and hydrogen bonding. Fe^{2+} from Fe-CPNWs also interacted with oxygen-containing functional groups of GO and CF, reinforcing their interactions. From Fig. S2, it is seen that the formed CF/GO/Fe-CPNW composite at the bottom of the beaker is visually homogeneous.

A free-standing CF/GO/Fe-CPNW paper was produced by vacuum-filtration-induced assembly. After carbonization, Fe-CPNWs were transformed into Fe_3O_4@C nanowires (Fe_3O_4@CNWs) and elimination of oxygen-containing functional groups converted GO into rGO, leading to the formation of free-standing CF/rGO/Fe_3O_4@CNWs hybrid paper. Figure 1a illustrates typical preparation process of the hybrid paper. Figure 1b shows that the resultant hybrid paper has a smooth surface. After bending, rolling and folding, the paper could maintain its structural integrity, exhibiting flexibility and superior mechanical property. It is noted that the control sample S0, without addition of CF, was prone to fracture into small pieces as shown in Fig. S3. Hence, it is inferred that CF played a role in strengthening mechanical property and improving flexibility of the paper.

The microstructures of hybrid paper are shown in Fig. 2. The cross-sectional view of the hybrid paper in Fig. 2a exhibits its thickness of about 363 μm, consisting of multiple layers. The thickness of the paper could be tuned

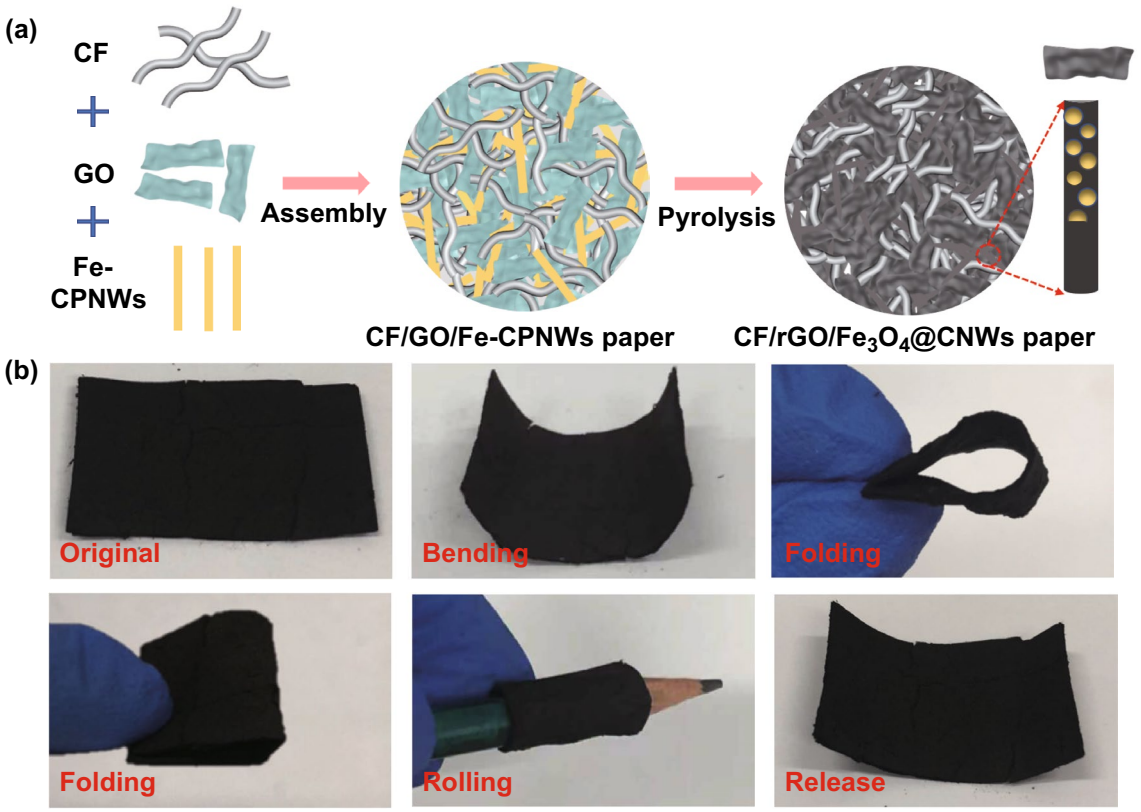

Fig. 1 **a** Preparation process of CF/rGO/Fe_3O_4@CNW hybrid paper. **b** Digital images showing flexible features of the CF/rGO/Fe_3O_4@CNW paper

 https://doi.org/10.1007/s40820-020-00461-x

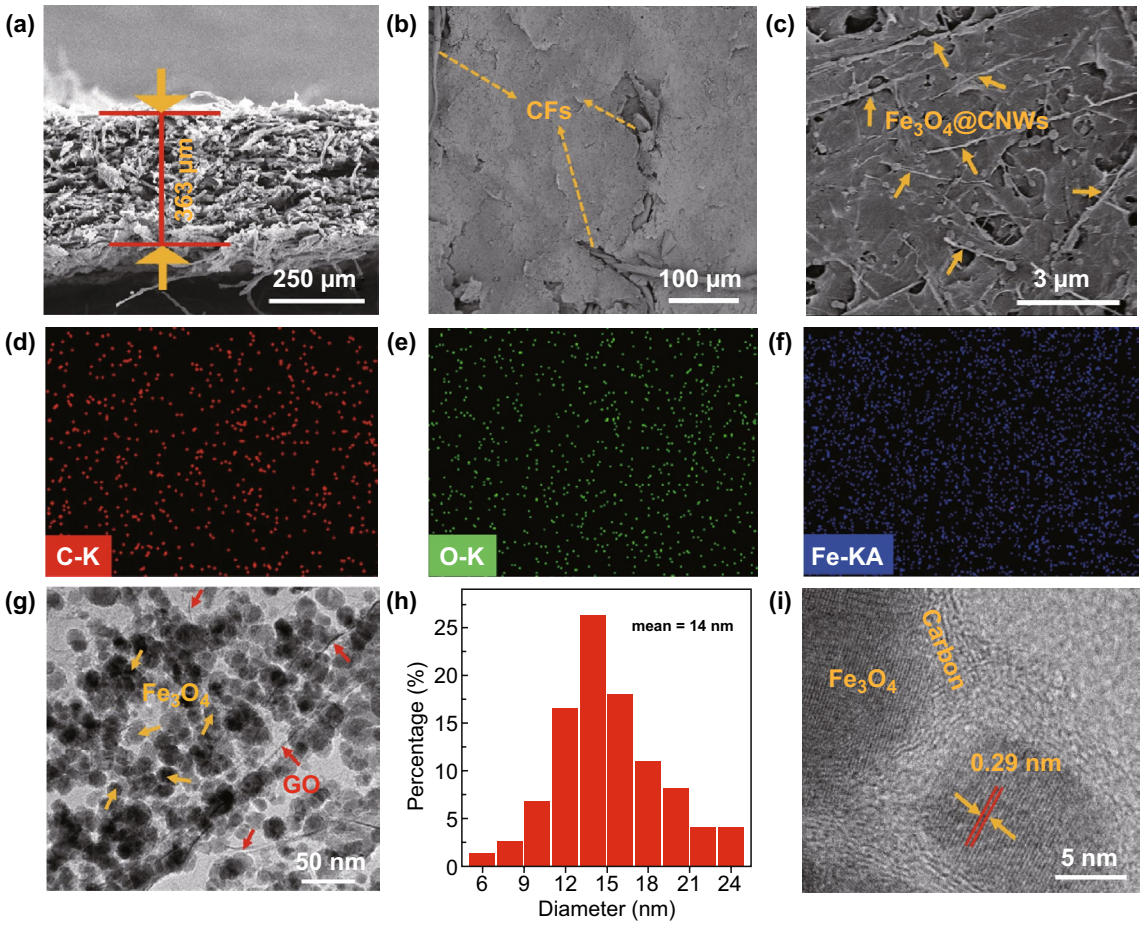

Fig. 2 **a** Cross-sectional view and **b–c** top-view FESEM images. **d–f** Elemental mapping of the hybrid paper. **g** TEM image of the hybrid paper. **h** Size distribution of Fe_3O_4 nanoparticles. **i** HRTEM image of the hybrid paper

between 206 and 449 μm by changing the CF content (Fig. S4). Figure 2b, c demonstrates that the CFs were surrounded by Fe_3O_4@CNW and rGO components, forming a relatively flat surface. A close inspection reveals that one-dimensional Fe_3O_4@CNWs and rGO nanosheets were tangled with each other. The energy-dispersive X-ray spectroscopy (EDS) spectrum shows strong signals from C, O and Fe elements (Fig. S5). The corresponding elemental mapping reveals that three elements Fe, C and O are evenly distributed throughout the paper (Fig. 2d–f). TEM images (Fig. 2g) reveal numerous Fe_3O_4@C nanostructures were intertwined with rGO. As shown in Fig. 2h, the mean diameter of Fe_3O_4 nanoparticles (NPs) is about 14 nm. The core–shell structure of Fe_3O_4@C could be observed from high-resolution TEM images in Fig. 2i. The lattice fringe spacing of ~ 0.29 nm corresponds to d-spacing of Fe_3O_4 {220} crystal planes [23].

XRD patterns in Fig. 3a reveal the structural information of all samples. The characteristic diffraction peaks of magnetite Fe_3O_4 could be found in all samples. The signals at 2θ values of 30.1°, 35.4°, 37.0°, 43.1°, 53.4°, 56.9°, 62.5° and 73.9° can be attributed to (220), (311), (222), (400), (422), (511), (440) and (533) crystal planes of Fe_3O_4 (JCPDS No. 19-0629), respectively [24]. It is noted that no characteristic diffraction peaks of carbon could be spotted in the XRD patterns owing to the low loading of rGO and the low crystallinity of CF, which was confirmed by Raman spectra.

In Fig. 3b, all samples show two prominent peaks at about 1357 and 1539 cm^{-1}, which correspond to D and G bands of carbon materials, respectively [25]. Generally, the intensity ratio of D band to G band (I_D/I_G) is utilized to assess the degree of disorder in the carbon-based components. Herein, the values of I_D/I_G are 0.92, 1.05, 1.07 and 1.10 for S0, S1, S2 and S3, respectively. With increasing content of CF, I_D/I_G

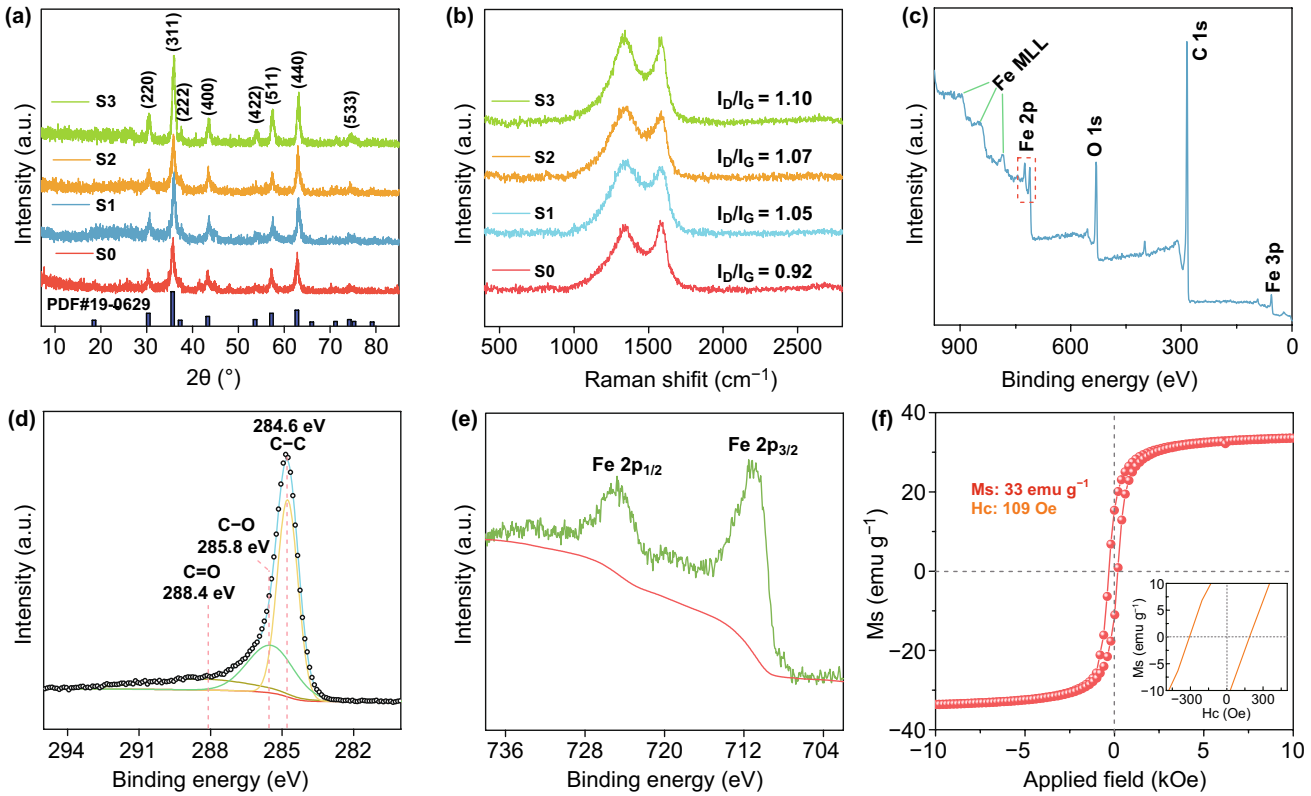

Fig. 3 **a** XRD patterns and **b** Raman spectra of all samples. **c** XPS broad survey. **d** C 1 s and **e** Fe 2p spectra of S2. **f** Magnetic hysteresis loop of S2 measured at room temperature

ratio increases gradually from S0 to S3, indicating increased disorder in the carbon-based components and further confirming the low crystallization degree of CF.

Due to similarity in XRD patterns between magnetite and maghemite [26]. XPS was carried out to provide insights into the elemental composition of the product and the oxidation state of each element. The total survey (Fig. 3c) shows that Fe, C and O elements were present on the surface of composite film. The O elements could be attributed to the residual oxygen-containing functional groups of GO. High-resolution C 1 s spectrum (Fig. 3d) was deconvoluted into three subpeaks corresponding to C–C (284.5 eV), C-O (285.8 eV) and C = O (288.4 eV) [27]. Fe 2p spectrum (Fig. 3e) shows two broad peaks at 710 and 724 eV, which can be ascribed to the ionization of Fe $2p_{3/2}$ and Fe $2p_{1/2}$. No satellite peak could be found at around 719.2 eV, which indicates that the as-synthesized Fe_3O_4 nanoparticles have high level of purity [28].

TG analysis was carried out in air to evaluate the content of Fe_3O_4. Due to oxidation of Fe^{2+}, the residue is comprised of Fe_2O_3 with mass percentage of about 60 wt% (Fig. S6) on the basis of Eq. 1:

$$Fe_3O_4(wt\%) = Residue(wt\%) \times \frac{2M_{Fe_3O_4}}{3M_{Fe_2O_3}} \quad (1)$$

Hence, it is inferred that the content of Fe_3O_4 in the hybrid paper is ~56 wt%. Fe_3O_4 could endow the paper with typical magnetic properties as proven in Fig. 3f. The representative sample S2 has a saturation magnetization (M_s) value of 33 emu g^{-1} and a coercive force of 190 Oe. The apparent magnetic behavior would bring about magnetic loss that dissipates EM waves [29].

RL values of samples were calculated using measured parameters, namely relative complex permittivity (ε_r) and relative complex permeability (μ_r). Based on the transmission line theory, RL can be calculated using Eqs. 2 and 3 [30, 31]:

$$Z_{in} = Z_0\sqrt{\frac{\mu_r}{\varepsilon_r}}\tanh\left[j\left(\frac{2f\pi t}{c}\right)\sqrt{\mu_r\varepsilon_r}\right] \quad (2)$$

https://doi.org/10.1007/s40820-020-00461-x

$$\mathrm{RL} = 20\log\left|\frac{Z_{in} - Z_0}{Z_{in} + Z_0}\right| \quad (3)$$

where Z_{in} is the input impedance of the absorber, Z_0 is the impedance of the free space, f is the microwave frequency, d is the thickness of absorber and c is the velocity of light. EM wave attenuation at an input wave frequency is considered adequate if RL value is below − 10 dB, representing attenuation of more than 90% of the incident EM energy [32]. The frequency ranges with RL below − 10 dB are defined as effective absorption frequency bandwidth (f_e). Figure 4 shows maximum *RL* (RL_{max}) and f_e values of all samples

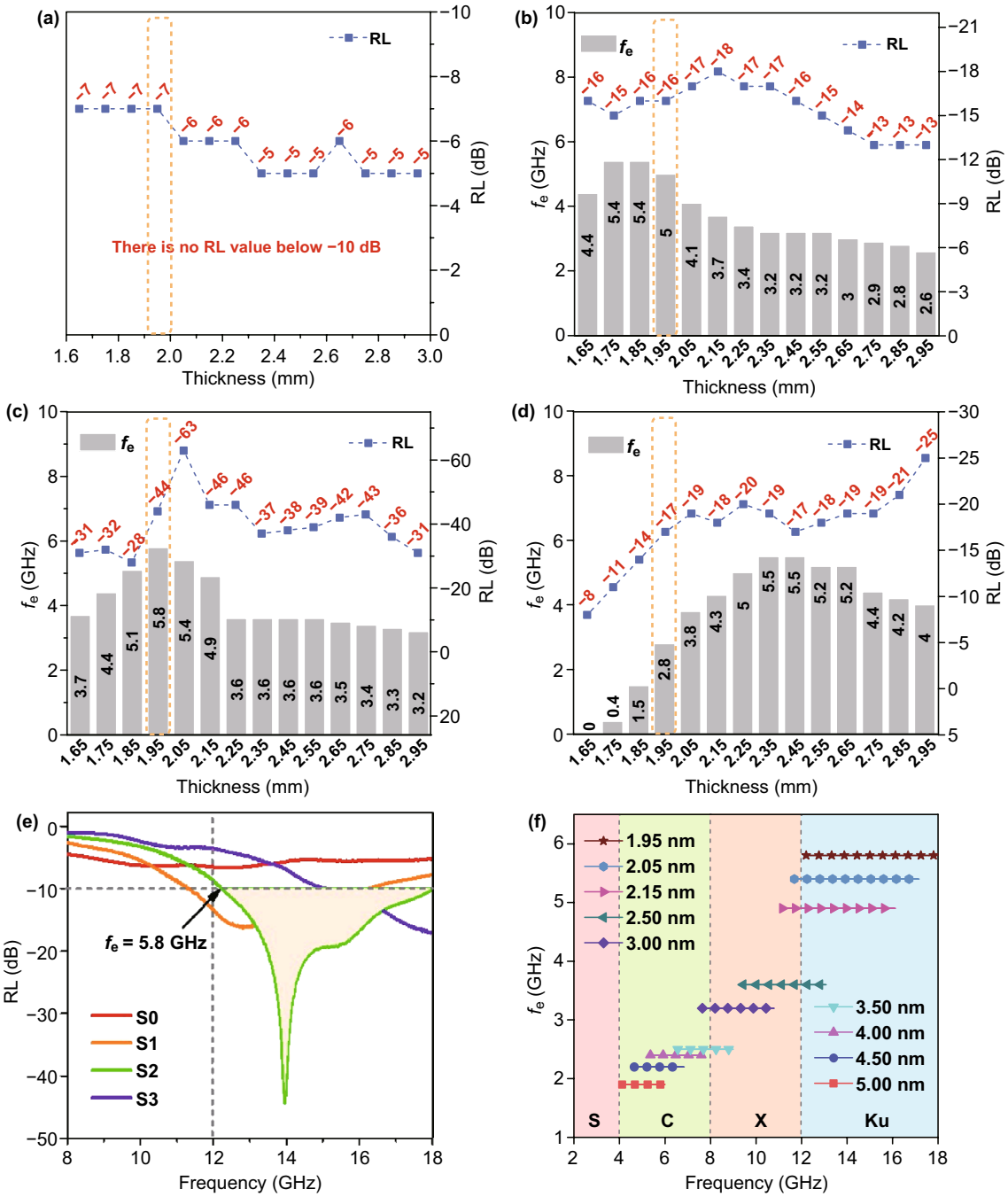

Fig. 4 Maximum *RL* and f_e values of **a** S0, **b** S1, **c** S2 and **d** S3. **e** RL curves of all samples at the thickness of 1.95 mm. **f** Effective absorption frequency bandwidths of S2 with various thicknesses between 1.95 and 5.00 mm

at different thickness. In Fig. 4a, none of the maximum RL values exceeds -10 dB (in magnitude) in S0. When CF was introduced, the microwave absorption performance was remarkably enhanced, as exemplified by S1 that showed a RL_{max} of -18 dB and broad f_e of 5.4 GHz at thicknesses of 2.15 mm and 1.75 mm, respectively (Fig. 4b). With increased CF content, RL_{max} of S2 could reach −63 dB at 2.05 mm and f_e was as high as 5.8 GHz at 1.95 mm (Fig. 4c). Further increase in CF content has resulted in lower RL_{max} of −25 dB and narrower maximum f_e of 5.5 GHz in S3, suggesting weakened absorption behavior (Fig. 4d). Among the four samples, S2 demonstrated the best microwave absorption capacity. Notably, the broad f_e of 5.8 GHz could cover the Ku band almost entirely at thickness of as low as 1.95 mm (Fig. 4e). When the thickness was tuned between 1.95 and 5.00 mm, the accumulated attenuated frequency range could nearly cover the entirety of C, X and Ku bands (Fig. 4f).

EM wave absorption properties are highly associated with the relative complex permittivity ($\varepsilon_r = \varepsilon' - j\varepsilon''$) and relative complex permeability ($\mu_r = \mu' - j\mu''$). In general, the real parts of complex permittivity (ε') and complex permeability (μ') represent the abilities of a material to store electric energy and magnetic energy, respectively, whereas the imaginary parts of the two quantities (ε'' and μ'') represent its abilities for electric energy dissipation and magnetic energy loss, respectively [33, 34]. In Fig. 5a, ε' and ε'' values of all samples decrease with increasing frequency due to typical frequency dispersion behavior, in which polarization lag is aggravated by electric field change at higher frequency [35]. Among them, S0 shows the highest ε' (ranging from 27.8 to 7.6) and ε'' (ranging from 27.1 to 8.9) values. When CF was introduced, both ε' and ε'' values of samples decreased with increasing CF content, possibly due to the reduction in conductive loss. According to the conductive-network model proposed by Cao and his coworker, the conductivity of the composite is significantly influenced by electron hopping between Fe_3O_4-rGO layers [36]. When CFs with low degree of graphitization is introduced, the CFs will behave like resistors, hindering interlayer electron hopping and intralayer electron migration, causing the conductive network to be less connected and decreasing conductance of the composite.

According to the Debye theory, ε_r can be expressed by the following equation in terms of $\omega = 2\pi f$ where f is frequency [37]:

$$\varepsilon_r = \varepsilon' - j\varepsilon'' = \varepsilon_\infty + \frac{\varepsilon_s - \varepsilon_\infty}{1 + j\omega\tau_0} \quad (4)$$

where τ_0, ε_∞ and ε_s are relaxation time, dielectric constant at infinite frequency and static dielectric constant, respectively. From Eq. 4, it can be inferred that

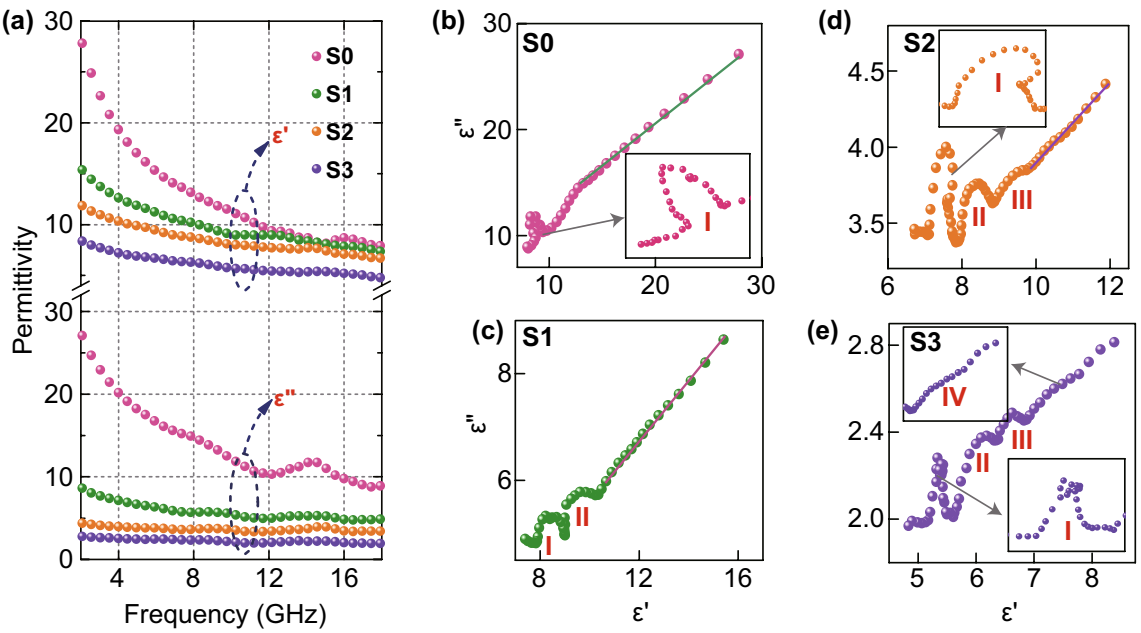

Fig. 5 **a** Plot of complex permittivity versus frequency and **b–e** Cole–Cole plots of all samples

https://doi.org/10.1007/s40820-020-00461-x

$$\varepsilon' = \varepsilon_\infty + \frac{\varepsilon_s - \varepsilon_\infty}{1 + (\omega\tau_0)^2} \quad (5)$$

$$\varepsilon'' = \frac{\omega\tau_0(\varepsilon_s - \varepsilon_\infty)}{1 + (\omega\tau_0)^2} \quad (6)$$

From Eqs. 5 and 6, the relationship between ε′ and ε″ can be further deduced as Eq. 7:

$$(\varepsilon' - \varepsilon_\infty)^2 + (\varepsilon'')^2 = (\varepsilon_s - \varepsilon_\infty)^2 \quad (7)$$

Therefore, the plot of ε″ versus ε′ would form either one or several semicircles, generally referred to as Cole–Cole semicircles, with each semicircle associated with one relaxation process [38]. Figure 5b–e shows curves of ε″ versus ε′ for each as-prepared hybrid paper. Distinct semicircles demonstrate the occurrence of relaxation processes in EM energy decay that could be ascribed to the presence of functional groups in rGO and multiple heterojunction interfaces including CF/rGO, Fe_3O_4@CNW/rGO, Fe_3O_4/C and Fe_3O_4@CNW/CF. The functional group can work as the dipolar site under the action of EM wave, causing dipolar polarization [39]. Che et al. revealed that the multiple heterojunction would lead to the accumulation and uneven distribution of charges at these interfaces, leading to the production of macroscopic electric moment. This would induce interfacial polarization and decay the incident EM energy [40]. There are one, two, three and four semicircles in S0, S1, S2 and S3, respectively. The increase in the number of semicircles indicates enhancement of the relaxation processes with the increase in CF content. This is attributed to the formation of more heterojunctions within the composite at which more charges could be accumulated with the increase in CF content, enhancing interfacial polarization. An obvious resonance peak of ε'' at about 14 GHz in S3 further illustrates its strong interfacial polarization. Meanwhile, with the increase in CF content, the slope of ε''-ε' curves became smoother, indicating decrease in conductivity [41].

From Fig. 6a, it is found that CF content has no significant effect on μ' and μ'' values of the composite. μ' and μ'' vary in the ranges of 0.92–1.07 and -0.08–0.18, respectively. However, the apparent resonance peaks could be found in the plot of μ'' against frequency, indicating magnetic loss caused by the Fe_3O_4. Low-frequency resonance peaks are usually related to natural resonance, whereas high-frequency resonance peaks may correspond to the exchange resonance [42]. Besides, eddy loss is another pathway for magnetic loss. According to previous reports, if the eddy loss contributes to magnetic loss, eddy current coefficient C_0 ($C_0 = \mu''(\mu')^{-2}f^{-1}$) will remain constant with variation in frequency [43]. From Fig. S7, C_0 of all samples rapidly decreased between the frequencies of 2 GHz and 8 GHz, fluctuated in frequency range of 8–13 GHz and remained constant in the range of 13–18 GHz, suggesting that eddy current loss contributed to microwave attenuation in Ku band.

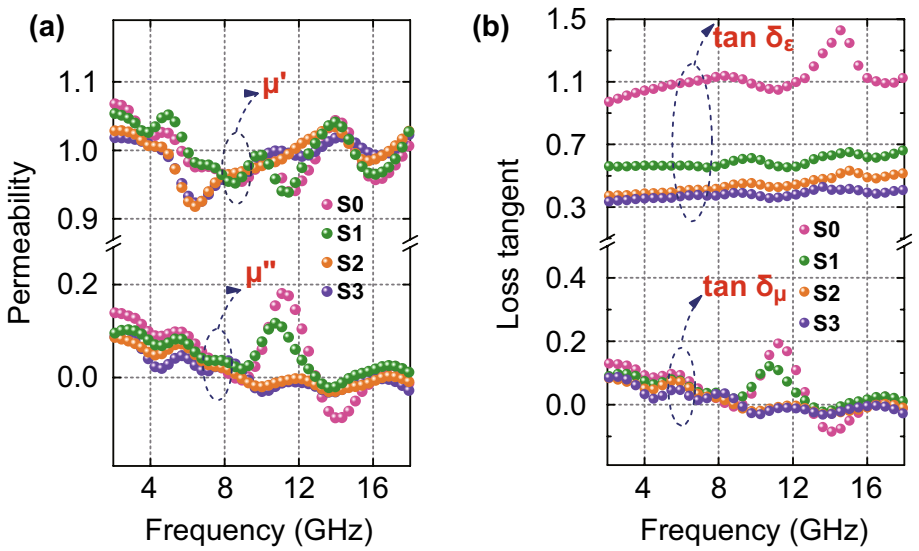

Fig. 6 **a** Complex permeability and **b** dielectric and magnetic loss tangents of all samples

Dielectric loss tangent (tan δ_ε) and magnetic loss tangent (tan δ_μ) were also evaluated and plotted as functions of frequency. As shown in Fig. 6b, tan δ_ε values of the composites are greater than their tan δ_μ values, which implies that dielectric loss was the dominant mechanism in EM energy attenuation for the composite [44]. As the CF content increased, the value of tan δ_ε decreased rapidly, while tan δ_μ values did not change significantly, indicating that CF content had no significant influence on magnetic loss. This phenomenon provides opportunity to improve impedance matching, facilitating penetration and attenuation of EM waves.

Figure 7a shows impedance matching values $|Z_{in}/Z_0|$ of all samples. Generally, when the impedance matching ratio $|Z_{in}/Z_0|$ is close to 1, almost all incident EM waves could penetrate the surface of a material with near-zero microwave reflection, presenting an ideal impedance matching [45]. S0 sample has a low $|Z_{in}/Z_0|$ value, resulting in poor impedance matching. However, with the increase in CF content, $|Z_{in}/Z_0|$ values increased significantly. In particular, $|Z_{in}/Z_0|$ of S2 fluctuated around 1, showing excellent impedance matching. When the EM waves penetrate the interior region, the energy should be dissipated as much as possible. The ability of a material to dissipate or attenuate EM energy of a frequency is described by its attenuation constant (α) [46]. As shown in Fig. 7b, α values of all samples exceeded 150 at high frequencies, suggesting strong microwave attenuation capability of these composites. This should be attributed to the synergistic effect of both dielectric and magnetic losses. Hence, the superior microwave absorption capability of S2 should be attributed to the optimal combination of good impedance matching and adequately high attenuation capacity. Table 1 summarizes the EM absorption performance of some representative carbon-based magnetic absorbers in the recent literature [36, 47–54]. It is noteworthy that the strong microwave

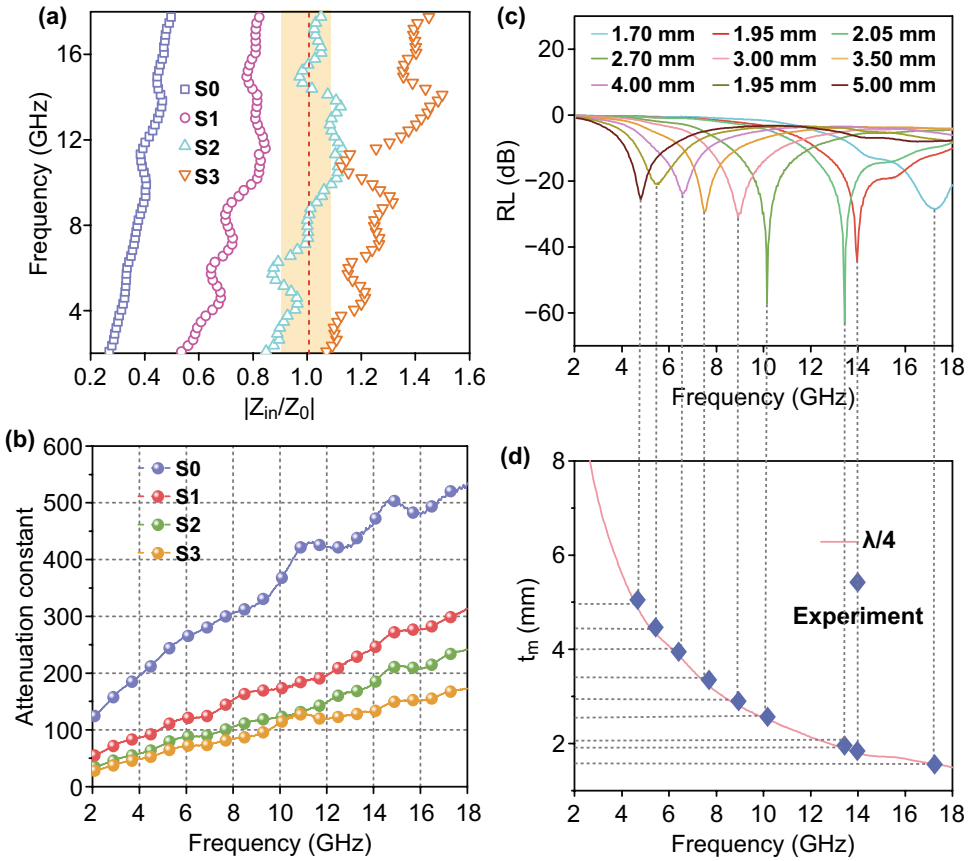

Fig. 7 **a** Attenuation constant and **b** $|Z_{in}/Z_0|$ values of all samples. **c** Plots of RL versus microwave frequency at different thicknesses of S2. **d** Relationship between simulated matching thickness t_m and peak frequency for S2

https://doi.org/10.1007/s40820-020-00461-x

Table 1 EM absorption properties of recently reported carbon-based magnetic absorbers and S2 sample in this work

Sample	Maximum RL value		Filler content	RL≦–10 dB		References
	D_m	RL_{max}		D_m	f_e	
Fe_3O_4/GCs	3.5	−32	30	3.5	~4.6	[47]
Fe_3O_4 clusters-NG	4.1	−53.6	30	1.8	~5	[36]
WPC/MNPs-80	2.0	−47.9	33	2.0	4.1	[48]
Co@C nanofiber	2.4	−40	50	2.4	~2.5	[49]
Porous carbon/Fe_3O_4@Fe	2.0	−49.6	30	2.0	5.0	[50]
Fe@NPC@CF	2.5	−46.2	25	2.5	5.2	[51]
Nanoporous carbon	2.0	−42.4	70	2.0	1.76	[52]
$FeNi_3$/N-GN	1.45	−57.2	50	1.94	4.2	[53]
Fe_3O_4@NPC	3.0	−65.5	40	3.0	4.5	[54]
S2	2.05	−63	20	1.95	5.8	This work

absorption of S2 at a low filler content of 20% is competitive to those reported EM absorbers.

To understand the relationship between thickness and peak frequency (*i.e.,* microwave frequency for which maximum RL was recorded for a given absorber thickness), the curves of RL versus frequency for S2 at different thicknesses are plotted in Fig. 7c. It is obvious that the peak shifts toward lower frequencies with increasing matching thickness, which can be explained by the quarter-wavelength cancelation model expressed by Eq. 8 [55, 56]:

$$t_m = n\lambda/4 = nc/(4f_m\sqrt{\mu_r\varepsilon_r}) \quad (n = 1, 3, 5 \ldots) \tag{8}$$

where c is the speed of EM waves in free space, t_m is matching thickness and f_m is matching (or peak) frequency. When the values of t_m and f_m satisfy this equation, EM waves reflected at air–absorber interface and EM waves reflected at absorber–device interface would be 180° out of phase, causing them to be canceled out due to destructive interference and leading to the high RL value [57]. In this case, peak frequencies and their corresponding matching thicknesses are proven to be consistent with the simulated values deduced from Eq. 8 (as shown in Fig. 7d). Hence, the quarter-wavelength cancelation model is vital to predict the absorption frequency and thickness of maximum RL for an EM absorber [58].

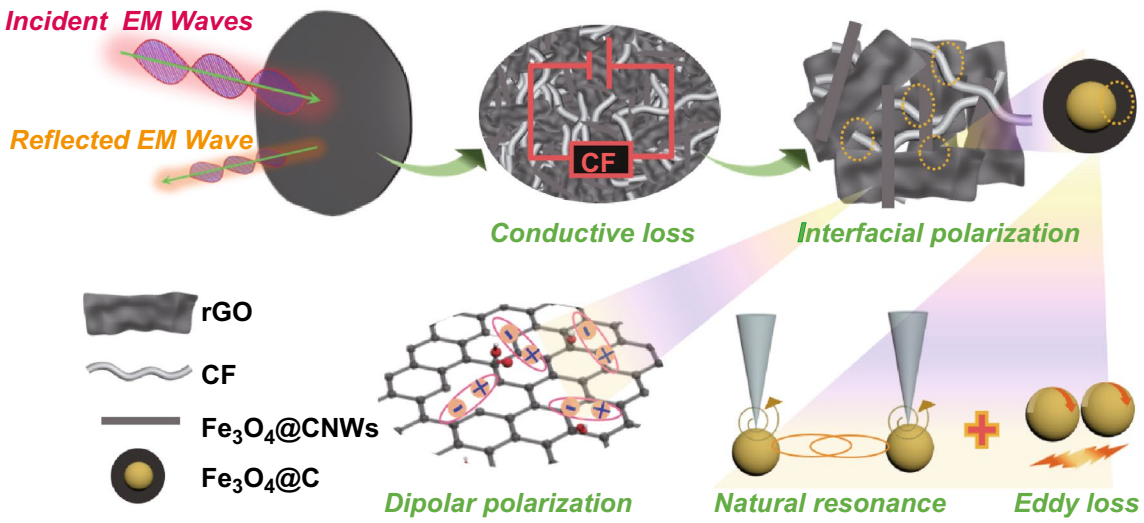

Fig. 8 Possible microwave absorption mechanisms for CF/rGO/Fe_3O_4@CNW hybrid paper

Based on the above discussion, the mechanisms of microwave absorption in CF/rGO/Fe_3O_4@CNW hybrid paper can be summarized in Fig. 8. Firstly, a maximized fraction of incoming EM waves (particularly microwaves) penetrated the air–absorber interface with a good impedance matching. Then, energy of the penetrated EM waves decayed through various mechanisms, expounded as follows:

(a) Conductive loss. In the composite, rGO nanosheets, Fe_3O_4@CNWs and CF formed a conductive network with finite resistance. As the incident EM wave propagated through the resistive conductive network, the induced microcurrent was rapidly attenuated in the resistive network and converted to thermal energy, leading to the decaying of penetrated EM energy.
(b) Polarization loss. Various phase boundaries in Fe_3O_4@CNW-rGO-CF could accumulate the charges, inducing interfacial polarization. Meanwhile, oxygen-containing functional group residues and defects in rGO could work as dipolar centers, causing dipolar polarization. Two kinds of polarization process could attenuate the incident EM wave.
(c) Magnetic loss. Natural resonance, exchange resonance and eddy loss resulting from the magnetic properties of the Fe_3O_4 core in Fe_3O_4@CNW contribute to the magnetic energy loss of the hybrid paper.

4 Conclusion

In summary, a lightweight and flexible CF/rGO/Fe_3O_4@CNW hybrid paper has been successfully fabricated through a vacuum filtration assembly process. Therein, carbon fibers (CFs) work as flexible backbone, tightly wrapped by the other dielectric and magnetic components including reduced graphene oxide (rGO) and Fe_3O_4@C nanowires (Fe_3O_4@CNWs). The strongest microwave absorption intensity of -63 dB can be achieved at a thickness of 2.05 mm, while the largest effective absorption bandwidth f_e is 5.8 GHz with a thickness as low as 1.95 mm. The fabrication approach for such a hybrid EM absorption paper with flexibility and lightweight features provides a promising way for the future development of lightweight and effective microwave absorbers.

Acknowledgements We are thankful for financial support from National Natural Science Foundation of China (No.: 51971111), the National Research Foundation, Prime Minister's Office, Singapore under its Campus for Research Excellence and Technological Enterprise (CREATE) program, the Funding for Outstanding Doctoral Dissertation in NUAA (No. BCXJ17-07), Postgraduate Research & Practice Innovation of Jiangsu Province (KYCX17_0252) and the Open Research Fund of Jiangsu Provincial Key Laboratory of Bionic Functional Materials.

Electronic supplementary material The online version of this article (https://doi.org/10.1007/s40820-020-00461-x) contains supplementary material, which is available to authorized users.

References

1. J. Liu, H. Zhang, X. Xie, R. Yang, Z. Liu, Y. Liu, Z. Yu, Multifunctional, superelastic, and lightweight MXene/polyimide aerogels. Small **14**, 1802479 (2018). https://doi.org/10.1002/smll.201802479
2. H. Lv, Z. Yang, P.L. Wang, G. Ji, J. Song, L. Zheng, H. Zeng, Z.J. Xu, A voltage-boosting strategy enabling a low-frequency, flexible electromagnetic wave absorption device. Adv. Mater. **30**(15), 1706343 (2018). https://doi.org/10.1002/adma.201706343
3. D.A. Gopakumar, A.R. Pai, Y.B. Pottathara, D. Pasquini, Cellulose nanofiber-based polyaniline flexible papers as sustainable microwave absorbers in the X-band. ACS Appl. Mater. Interfaces **10**, 20032–20043 (2018). https://doi.org/10.1021/acsami.8b04549
4. P. Liu, C. Zhu, S. Gao, C. Guan, Y. Huang, W. He, N-doped porous carbon nanoplates embedded with CoS_2 vertically anchored on carbon cloths for flexible and ultrahigh microwave absorption. Carbon **163**, 348–359 (2020). https://doi.org/10.1016/j.carbon.2020.03.041
5. Z. Lou, R. Li, P. Wang, Y. Zhang, B. Chen et al., Phenolic foam-derived magnetic carbon foams (MCFs) with tunable electromagnetic wave absorption behavior. Chem. Eng. J. (2019). https://doi.org/10.1016/j.cej.2019.123571
6. H. Sun, R. Che, X. You, Y. Jiang, Z. Yang, J. Deng, L. Qiu, H. Peng, Cross-stacking aligned carbon-nanotube films to tune microwave absorption frequencies and increase

absorption intensities. Adv. Mater. **26**, 8120–8125 (2014). https://doi.org/10.1002/adma.201403735

7. B. Zhao, S. Zeng, X. Li, X. Guo, Z. Bai, B. Fan, R. Zhang, Flexible PVDF/carbon materials/Ni composite films maintaining strong electromagnetic wave shielding under cyclic microwave irradiation. J. Mater. Chem. C **8**, 500–509 (2020). https://doi.org/10.1039/C9TC05462F
8. L. Huang, J. Li, Y. Li, Y. Li, X. He, Y. Yuan, Lightweight and flexible hybrid film based on delicate design of electrospun nanofibers for high-performance electromagnetic interference shielding. Nanoscale **11**(17), 8616 (2019). https://doi.org/10.1039/c9nr02102
9. H. Zhang, G. Zhang, M. Tang, L. Zhou, J. Li, X. Fan, X. Shi, J. Qin, Synergistic effect of carbon nanotube and graphene nanoplates on the mechanical, electrical and electromagnetic interference shielding properties of polymer composites and polymer composite foams. Chem. Eng. J. **353**, 381–393 (2018). https://doi.org/10.1016/j.cej.2018.07.144
10. X. Li, L. Wang, W. You, L. Xing, L. Yang, X. Yu, J. Zhang, Y. Li, R. Che, Enhanced polarization from flexible hierarchical MnO_2 arrays on the cotton cloth with excellent microwave absorption. Nanoscale **11**, 13269–13281 (2019). https://doi.org/10.1039/c9nr02667c
11. L. Wang, X. Li, Q. Li, X. Yu, Y. Zhao, J. Zhang, M. Wang, R. Che, Oriented polarization tuning broadband absorption from flexible hierarchical ZnO arrays vertically supported on carbon cloth. Small **15**, 1900900 (2019). https://doi.org/10.1002/smll.201900900
12. P. Cataldi, L. Ceseracciu, A. Athanassiou, I.S. Bayer, Healable cotton-graphene nanocomposite conductor for wearable electronics. ACS Appl. Mater. Interfaces **9**(16), 13825–13830 (2017). https://doi.org/10.1021/acsami.7b02326
13. H. Zhao, Y. Cheng, J. Ma, Y. Zhang, G. Ji, Y. Du, A sustainable route from biomass cotton to construct lightweight and high performance microwave absorber. Chem. Eng. J. **339**, 432–441 (2018). https://doi.org/10.1016/j.cej.2018.01.151
14. L. Yang, M. Li, Y. Zhang, J. Liu, Z. Yang, Multiple polarization effect of shell evolution on hierarchical hollow C@MnO_2 composites and their wideband electromagnetic wave absorption properties. Chem. Eng. J. **392**, 123666 (2020). https://doi.org/10.1016/j.cej.2019.123666
15. H. Zhao, Y. Cheng, W. Liu, L. Yang, B. Zhang et al., Biomass-derived porous carbon-based nanostructures for microwave absorption. Nano-Micro Lett. **11**, 24 (2019). https://doi.org/10.1007/s40820-019-0255-3
16. M. Cao, C. Han, X. Wang, M. Zhang, Y. Zhang et al., Graphene nanohybrids: excellent electromagnetic properties for the absorbing and shielding of electromagnetic waves. J. Mater. Chem. C **6**, 4586–4602 (2018). https://doi.org/10.1039/c7tc05869a
17. G. Wang, Z. Gao, G. Wan, S. Lin, P. Yang, Y. Qin, High densities of magnetic nanoparticles supported on graphene fabricated by atomic layer deposition and their use as efficient synergistic microwave absorbers. Nano Res. **7**(5), 704–716 (2014). https://doi.org/10.1007/s12274-014-0432-0
18. L. Qin, W. Lv, W. Wei, F. Kang, D. Zhai, Q. Yang, Oxygen-enriched carbon nanotubes as a bifunctional catalyst promote the oxygen reduction/evolution reactions in Li-O_2 batteries. Carbon **141**, 561–567 (2019). https://doi.org/10.1016/j.carbon.2018.10.025
19. Z. Li, Z. Jia, T. Ni, S. Li, Adsorption of methylene blue on natural cotton based flexible carbon fiber aerogels activated by novel air-limited carbonization method. J. Mol. Liq. **242**, 747–756 (2017). https://doi.org/10.1016/j.molliq.2017.07.062
20. Y. He, J. Li, L. Li, J. Li, Gamma-ray irradiation-induced reduction and self-assembly of graphene oxide into three-dimensional graphene aerogel. Mater. Lett. **3**, 1365–1371 (2016). https://doi.org/10.1016/j.matlet.2016.04.187
21. C. Li, L. Mei, L. Chen, Q. Li, T. Wang, Synthesis of highly aligned and ultralong coordination polymer nanowires and their calcination to porous manganese oxide nanostructures. J. Mater. Chem. **22**(48), 4982 (2012). https://doi.org/10.1039/C2JM15607E
22. H. Wang, S. Zhou, Y. Liang, X. Han, B. Zhang, General self-template synthesis of transition-metal oxide and chalcogenide mesoporous nanotubes with enhanced electrochemical performances. Angew. Chem. Int. Ed. **55**(31), 9055 (2016). https://doi.org/10.1002/anie.201603197
23. M. Lu, M. Cao, Y. Chen, W. Cao, J. Liu et al., Multiscale assembly of grape-like ferro ferric oxide and carbon nanotubes: a smart absorber prototype varying temperature to tune intensities. ACS Appl. Mater. Interfaces **7**, 19408–19415 (2015). https://doi.org/10.1039/c2jm15607e
24. Y. Cheng, J. Cao, Y. Li, Z. Li, H. Zhao, G. Ji, Y. Du, The outside-in approach to construct Fe_3O_4 nanocrystals/mesoporous carbon hollow spheres core-shell hybrids toward microwave absorption. ACS Sustain. Chem. Eng. **6**, 1427–1435 (2018). https://doi.org/10.1021/acssuschemeng.7b03846
25. P. Liu, Y. Zhang, J. Yan, Y. Huang, L. Xia, Z. Guang, Synthesis of lightweight N-doped graphene foams with open reticular structure for high-efficiency electromagnetic wave absorption. Chem. Eng. J. **368**, 285–298 (2019). https://doi.org/10.1016/j.cej.2019.02.193
26. H. Lv, G. Ji, H. Zhang, Y.W. Du, Achieving hierarchical hollow carbon@Fe@Fe_3O_4 nanospheres with superior microwave absorption properties and lightweight features. J. Mater. Chem. C **39**, 10232–10241 (2015). https://doi.org/10.1039/C5TC02512E
27. P. Liu, S. Gao, Y. Wang, Y. Huang, W. He, W. Huang, J. Luo, Carbon nanocages with N-doped carbon inner shell and Co/N-doped carbon outer shell as electromagnetic wave absorption materials. Chem. Eng. J. **381**, 122653 (2020). https://doi.org/10.1016/j.cej.2019.122653
28. H. Zhao, Y. Cheng, W. Liu, Z. Yang, B. Zhang, G. Ji, Y. Du, The flaky porous Fe_3O_4 with tunable dimensions for enhanced microwave absorption performance in X and C bands. Nanotechnology **29**, 295603 (2018). https://doi.org/10.1088/1361-6528/aac0de
29. B. Zhao, X. Guo, W. Zhao, J. Deng, B. Fan, G. Shao, Z. Bai, R. Zhang, Facile synthesis of yolk–shell Ni@void@

SnO_2(Ni_3Sn_2) ternary composites via galvanic replacement/Kirkendall effect and their enhanced microwave absorption properties. Nano Res. **10**, 331–343 (2017). https://doi.org/10.1007/s12274-016-1295-3

30. P. Liu, S. Gao, X. Liu, Y. Huang, W. He, Y. Li, Rational construction of hierarchical hollow CuS@CoS_2 nanoboxes with heterogeneous interfaces for high-efficiency microwave absorption materials. Compos. Part B Eng. **192**, 107992 (2020). https://doi.org/10.1016/j.compositesb.2020.107992
31. Y. Cheng, H. Zhao, Y. Zhao, J. Cao, J. Zheng, G. Ji, Structure-switchable mesoporous carbon hollow sphere framework toward sensitive microwave response. Carbon **161**, 870–879 (2020). https://doi.org/10.1016/j.carbon.2020.02.011
32. P. Liu, S. Cao, Y. Wang, Y. Huang, Y. Wang, J. Luo, Core–shell CoNi@graphitic carbon decorated on B, N-Codoped hollow carbon polyhedrons toward lightweight and high-efficiency microwave attenuation. ACS Appl. Mater. Interfaces **11**, 25624–25635 (2019). https://doi.org/10.1021/acsami.9b08525
33. Y. Zhang, H. Zhang, X. Wu, Z. Deng, E. Zhou, Z. Yu, Nanolayered cobalt@carbon hybrids derived from metal – organic frameworks for microwave absorption. ACS Appl. Nano Mater. **2**, 2325–2335 (2019). https://doi.org/10.1021/acsanm.9b00226
34. Y. Cheng, Y. Zhao, H. Zhao, H. Lv, X. Qi, J. Cao, G. Ji, Y. Du, Engineering morphology configurations of hierarchical flower-like $MoSe_2$ spheres enable excellent low-frequency and selective microwave response properties. Chem. Eng. J. **372**, 390–398 (2019). https://doi.org/10.1016/j.cej.2019.04.174
35. H. Lv, Z. Yang, S.J.H. Ong, C. Wei, H. Liao et al., A flexible microwave shield with tunable frequency-transmission and electromagnetic compatibility. Adv. Funct. Mater. **29**, 1900163 (2019). https://doi.org/10.1002/adfm.201900163
36. X. Wang, T. Ma, J. Shu, M. Cao, Confinedly tailoring Fe_3O_4 clusters-NG to tune electromagnetic parameters and microwave absorption with broadened bandwidth. Chem. Eng. J. **332**, 321–330 (2018). https://doi.org/10.1016/j.cej.2017.09.101
37. X. Liang, Y. Cheng, H. Zhang, D. Tang, B. Tang, Y. Du, Coin-like α-Fe_2O_3@$CoFe_2O_4$ core-shell composites with excellent electromagnetic absorption performance. ACS Appl. Mater. Interfaces **7**, 4744–4750 (2015). https://doi.org/10.1021/am508438s
38. H. Lv, H. Zhang, J. Zhao, G. Ji, Y. Du, Achieving excellent bandwidth absorption by a mirror growth process of magnetic porous polyhedron structures. Nano Res. **9**, 1813–1822 (2016). https://doi.org/10.1007/s12274-016-1074-1
39. Z. Jia, K. Kou, S. Yin, A. Feng, C. Zhang, X. Liu, H. Cao, G. Wu, Magnetic Fe nanoparticle to decorate N dotted C as an exceptionally absorption-dominate electromagnetic shielding material. Compos. Part B: Eng. **189**, 107895 (2020). https://doi.org/10.1016/j.compositesb.2020.107895
40. Q. Liu, Q. Cao, H. Bi, C. Liang, K. Yuan, W. She, Y. Yang, R. Che, CoNi@SiO_2@TiO_2 and CoNi@Air@TiO_2 microspheres with strong wideband microwave absorption. Adv. Mater. **28**, 486–490 (2016). https://doi.org/10.1002/adma.201503149
41. R. Che, L. Peng, X. Duan, Q. Chen, X. Liang, Microwave absorption enhancement and complex permittivity and permeability of Fe encapsulated within carbon nanotubes. Adv. Mater. **16**(5), 401–405 (2004). https://doi.org/10.1002/adma.200306460
42. H. Zhao, Y. Cheng, H. Lv, G. Ji, Y. Du, A novel hierarchically porous magnetic carbon derived from biomass for strong lightweight microwave absorption. Carbon **142**, 245–253 (2019). https://doi.org/10.1016/j.carbon.2018.10.027
43. C. Zhou, C. Wu, D. Liu, M. Yan, Metal-organic framework derived hierarchical Co/C@V_2O_3 hollow spheres as a thin, lightweight, and high-efficiency electromagnetic wave absorber. Chem. Eur. J. **25**, 2234–2241 (2019). https://doi.org/10.1002/chem.201805565
44. X. Li, Z. Deng, Y. Li, H. Zhang, S. Zhao et al., Controllable synthesis of hollow microspheres with Fe@carbon dual-shells for broad bandwidth microwave absorption. Carbon **147**, 172–181 (2019). https://doi.org/10.1016/j.carbon.2019.02.073
45. Z. Deng, Y. Li, H. Zhang, Y. Zhang, J. Luo, L. Liu, Z. Yu, Lightweight Fe@C hollow microspheres with tunable cavity for broadband microwave absorption. Compos. Part B: Eng. **177**, 107346 (2019). https://doi.org/10.1016/j.compositesb.2019.107346
46. G. Zhao, H. Lv, Y. Zhou, X. Zheng, C. Wu, C. Xu, Self-assembled sandwich-like MXene-derived nanocomposites for enhanced electromagnetic wave absorption. ACS Appl. Mater. Interfaces **10**, 42925–42932 (2018). https://doi.org/10.1021/acsami.8b16727
47. X. Jian, B. Wu, Y. Wei, S.X. Dou, X. Wang, W. He, N. Mahmood, Facile synthesis of Fe_3O_4/GCs composites and their enhanced microwave absorption properties. ACS Appl. Mater. Interfaces **8**, 6101–6109 (2016). https://doi.org/10.1021/acsami.6b00388
48. J. Fang, T. Liu, Z. Chen, Y. Wang, W. Wei, X. Yue, Z. Jiang, A wormhole-like porous carbon/magnetic particles composite as an efficient broadband electromagnetic wave absorber. Nanoscale **8**, 8899–8909 (2016). https://doi.org/10.1039/C6NR01863G
49. J. Zhang, P. Wang, Y. Chen, G. Wang, D. Wang, L. Qiao, T. Wang, F. Li, Microwave absorption properties of Co@C nanofiber composite for normal and oblique incidence. J. Electron. Mater. **47**, 4703–4709 (2018). https://doi.org/10.1007/s11664-018-6351-1
50. H. Wang, F. Meng, J. Li, T. Li, Z. Chen, H. Luo, Z. Zhou, Carbonized design of hierarchical porous carbon/Fe_3O_4@Fe derived from loofah sponge to achieve tunable high-performance microwave absorption. ACS Sustain. Chem. Eng. **6**, 11801–11810 (2018). https://doi.org/10.1021/acssuschemeng.8b02089
51. X. Li, E. Cui, Z. Xiang, L. Yu, J. Xiong, F. Pan, W. Lu, Fe@NPC@CF nanocomposites derived from Fe-MOFs/biomass cotton for lightweight and high-performance electromagnetic wave absorption applications. J. Alloy. Compd. **819**, 152952 (2020). https://doi.org/10.1016/j.jallcom.2019.152952

 https://doi.org/10.1007/s40820-020-00461-x

52. X. Qiu, L. Wang, H. Zhu, Y. Guan, Q. Zhang, Lightweight and efficient microwave absorbing materials based on walnut shell-derived nanoporous carbon. Nanoscale **9**, 7408 (2017). https://doi.org/10.1039/c7nr02628e
53. J. Feng, Y. Zong, Y. Sun, Y. Zhang, X. Yang et al., Optimization of porous $FeNi_3$/N-GN composites with superior microwave absorption performance. Chem. Eng. J. **345**, 441–451 (2018). https://doi.org/10.1016/j.cej.2018.04.006
54. Z. Xiang, Y. Song, J. Xiong, Z. Pan, X. Wang et al., Enhanced electromagnetic wave absorption of nanoporous Fe_3O_4@carbon composites derived from metal-organic frameworks. Carbon **142**, 20–31 (2019). https://doi.org/10.1016/j.carbon.2018.10.014
55. X. Zhou, Z. Jia, A. Feng, J. Kou, H. Cao, X. Liu, Construction of multiple electromagnetic loss mechanism for enhanced electromagnetic absorption performance of fish scale-derived biomass absorber. Compos. Part B: Eng. **192**, 107980 (2020). https://doi.org/10.1016/j.compositesb.2020.107980
56. H. Lv, Z. Yang, H. Xu, L. Wang, R. Wu, An electrical switch-driven flexible electromagnetic absorber. Adv. Funct. Mater. **30**, 1907251 (2020). https://doi.org/10.1002/adfm.201907251
57. J. Fang, Y. Shang, Z. Chen, W. Wei, Y. Hu, X. Yue, Z. Jiang, Rice husk-based hierarchically porous carbon and magnetic particles composites for highly efficient electromagnetic wave attenuation. J. Mater. Chem. C **5**, 4695–4705 (2017). https://doi.org/10.1039/c7tc00987a
58. Z. Lou, C. Yuan, Y. Zhang, Y. Li, J. Cai et al., Synthesis of porous carbon matrix with inlaid Fe_3C/Fe_3O_4 micro-particles as an effective electromagnetic wave absorber from natural wood shavings. J. Alloys Compd. **775**, 800–809 (2020). https://doi.org/10.1016/j.jallcom.2018.10.213